HAL
open science

Thermoelectric and transport properties of Delafossite CuCrO2:Mg thin films prepared by RF magnetron sputtering

Inthuga Sinnarasa, Yohann Thimont, Lionel Presmanes, Antoine Barnabé, Philippe Tailhades

To cite this version:

Inthuga Sinnarasa, Yohann Thimont, Lionel Presmanes, Antoine Barnabé, Philippe Tailhades. Thermoelectric and transport properties of Delafossite CuCrO2:Mg thin films prepared by RF magnetron sputtering. Nanomaterials, 2017, 7 (7), pp.157. 10.3390/nano7070157 . hal-01754780

HAL Id: hal-01754780

https://hal.science/hal-01754780v1

Submitted on 30 Mar 2018

HAL is a multi-disciplinary open access archive for the deposit and dissemination of scientific research documents, whether they are published or not. The documents may come from teaching and research institutions in France or abroad, or from public or private research centers.

L'archive ouverte pluridisciplinaire **HAL**, est destinée au dépôt et à la diffusion de documents scientifiques de niveau recherche, publiés ou non, émanant des établissements d'enseignement et de recherche français ou étrangers, des laboratoires publics ou privés.

Open Archive TOULOUSE Archive Ouverte (OATAO)
OATAO is an open access repository that collects the work of Toulouse researchers and makes it freely available over the web where possible.

This is a publisher's version published in : http://oatao.univ-toulouse.fr/
Eprints ID : 19788

To link to this article : DOI:10.3390/nano7070157
URL : http://dx.doi.org/10.3390/nano7070157

To cite this version : Sinnarasa, Inthuga and Thimont, Yohann and Presmanes, Lionel and Tailhades, Philippe *Thermoelectric and transport properties of Delafossite CuCrO2:Mg thin films prepared by RF magnetron sputtering*. (2017) Nanomaterials, vol. 7 (n° 157). pp. 1-16. ISSN 2079-4991

Any correspondence concerning this service should be sent to the repository administrator: staff-oatao@listes-diff.inp-toulouse.fr

nanomaterials

MDPI

Article

Thermoelectric and Transport Properties of Delafossite $CuCrO_2$:Mg Thin Films Prepared by RF Magnetron Sputtering

Inthuga Sinnarasa, Yohann Thimont *, Lionel Presmanes, Antoine Barnabé and Philippe Tailhades

CIRIMAT, Université de Toulouse, CNRS, INPT, UPS, 118 route de Narbonne, F-31062 Toulouse CEDEX 9, France; sinnarasa@chimie.ups-tlse.fr (I.S.); presmanes@chimie.ups-tlse.fr (L.P.); barnabe@chimie.ups-tlse.fr (A.B.); tailhades@chimie.ups-tlse.fr (P.T.)

* Correspondence: thimont@chimie.ups-tlse.fr; Tel.: +33-561-557-292

Received: 24 May 2017; Accepted: 21 June 2017; Published: 27 June 2017

Abstract: P-type Mg doped $CuCrO_2$ thin films have been deposited on fused silica substrates by Radio-Frequency (RF) magnetron sputtering. The as-deposited $CuCrO_2$:Mg thin films have been annealed at different temperatures (from 450 to 650 °C) under primary vacuum to obtain the delafossite phase. The annealed samples exhibit 3R delafossite structure. Electrical conductivity σ and Seebeck coefficient S of all annealed films have been measured from 40 to 220 °C. The optimized properties have been obtained for $CuCrO_2$:Mg thin film annealed at 550 °C. At a measurement temperature of 40 °C, this sample exhibited the highest electrical conductivity of 0.60 $S \cdot cm^{-1}$ with a Seebeck coefficient of +329 $\mu V \cdot K^{-1}$. The calculated power factor ($PF = \sigma S^2$) was 6 $\mu W \cdot m^{-1} \cdot K^{-2}$ at 40 °C and due to the constant Seebeck coefficient and the increasing electrical conductivity with measurement temperature, it reached 38 $\mu W \cdot m^{-1} \cdot K^{-2}$ at 220 °C. Moreover, according to measurement of the Seebeck coefficient and electrical conductivity in temperature, we confirmed that $CuCrO_2$:Mg exhibits hopping conduction and degenerates semiconductor behavior. Carrier concentration, Fermi level, and hole effective mass have been discussed.

Keywords: thermoelectric; oxides; delafossite; thin film; power factor; degenerated semiconductor; hopping mode

1. Introduction

The thermoelectricity is a promising technique to overcome the issues in recovering waste heat to electricity without using moving parts. Thermoelectric (TE) effect is defined as the conversion of a temperature gradient directly into electricity and vice versa [1]. Thermoelectric generators have several advantages: they are particularly reliable, maintenance free, and durable with long operating life under extreme conditions [2].

The performance of the TE materials is described by the dimension less figure of merit ZT [1].

$$ZT = \frac{\sigma S^2}{(K_e + K_{th})} \times T \quad (1)$$

In these equations, σ and S are respectively the electrical conductivity and the Seebeck coefficient [3] at the given temperature T and K_e and K_{th} are respectively due to the electron transport and the lattice phonon at the given temperature T. The enhancement efforts of ZT is very challenging because of the σ, S, and K_e interdependence. Indeed, as the carrier density expands, the electrical conductivity increases and at the same time it reduces the Seebeck coefficient and increases the electronical thermal conductivity. To optimize TE materials, the Power Factor ($PF = \sigma S^2$) must be

increased without increasing the global thermal conductivity. This can be done by improving the carrier concentration and the mobility and/or reducing the lattice thermal conductivity K_{th} by introducing scattering centers with point defects [4], interfaces [5], and nanostructuration [6].

The advantage of the thin films versus bulk materials is rarely guested with the *PF*. Only the Figure of Merit (*ZT*) can reveal it. In fact some macroscopic disorder can lead to a significant reduction of the thermal conductivity of thin films relative to that observed in bulk material [7–9]. As *ZT* takes into account the thermal conductivity, thin films could have better TE properties than the bulk thanks to their microstructures. Moreover, the low dimension system obtained in thin films could make a significant band structure modification that could impact the Seebeck coefficient.

Transition metal oxides (TMOs) are a captivating class of materials due to their wide ranging electronic, chemical, and mechanical properties. Furthermore, they are gaining increasing attention for their thermoelectric (TE) properties due to their high temperature stability, tunable electronic and phonon transport properties, and well-established synthesis techniques.

Delafossite type oxides $Cu^{I}M^{III}O_2$ with M = (Fe, Al, Ga, Cr ...) due to their large range of properties and the abundance of their constituent elements in the nature, have been studied for several applications such as transparent p-type conducting oxides (TCO) [10–17], transparent electronic devices [18–25], dye-sensitized solar cells [26–29], and photoelectrodes [30] but also for outstanding catalysis [31] and photo-catalysis [31–41], antibacterial [42], luminescence [43–45], gas and temperature sensing [46–49], magnetic and electric [50–54], energy storage [55], oxygen storage [56], water reduction [57], thermoelectricity and superconductivity [58] properties. In the oxide family, the cation Cu^{I} is a monovalent metal and the cation M^{III} is a trivalent metal. Delafossite structure can be described as a stack of cation Cu^{I} layer and MO_6 octahedron layer along c axis. Each cation Cu^{I} is linearly coordinated to two oxygens belonging to upper and lower MO_6 octahedron. Even if Cu-based delafossite type oxides receive most of the attention for their optoelectronic properties as a p-type transparent semiconductor, they exhibit also interesting thermoelectric (TE) properties [59–67].

Among the Cu-based delafossites, $CuCrO_2$ is currently of interest due to its attractive physical properties for the applications mentioned above [68–78]. Hayashi et al. [69] studied TE properties of $CuCrO_2$ in bulk form with several dopants and reported that the Mg-doped samples showed a higher electrical conductivity leading to a higher power factor ($PF = 2.36 \times 10^{-4}$ $W \cdot m^{-1} \cdot K^{-2}$ at 820 °C) than the undoped bulk. In comparison with $CuCrO_2$ and $CuCrO_2$:Mg studies carried out on bulk materials [70,71,74,79,80], there is a lack of papers related to proper studies of the TE properties of $CuCrO_2$:Mg thin films, as for instance, the determination of *PF*. Most of the time, Seebeck measurements presented in the bibliography are only used to characterize the fundamental physical properties (type of charge carriers, transport mechanism) [16,73,81–85] especially because it is difficult to determine the main charge carrier characteristics by conventional Hall measurements in this type of material. In particular, we have measured the Seebeck coefficient at room temperature for 100 nm thick films in order to determine the type of the main charge carrier in $CuCrO_2$:Mg thin films optimized for TCO properties [16]. In the present article, the work is focused on the determination of electrical conductivities and TE properties (Seebeck coefficient and calculated power factor) in temperature ranging from 40 to 220 °C for one set of $CuCrO_2$ films annealed at various temperatures, with a fixed thickness of 300 nm.

2. Materials and Methods

2.1. Preparation of Mg-Doped $CuCrO_2$ (Target)

Polycrystalline $CuCr_{0.97}Mg_{0.03}O_2$ powder was prepared by grinding and mixing the starting commercial oxides, Cu_2O, Cr_2O_3, and MgO with appropriate proportions. The stoichiometric oxide mixture was annealed at 900 °C for 10 h in an ambient nitrogen atmosphere and cooled down to room temperature. After it was reground, the mixture was reheated for a further 10 h period. The purity of the phase was checked by X-Ray Diffraction (XRD).

The polycrystalline delafossite powder has been pressed into a sputtering target of 10 cm in diameter then sintered at 1200 °C for 10 h in air. The X-Ray Diffraction (XRD) analysis on a small representative pellet showed only the 3R delafossite phase. (R-3m space group with a = 2.9755(2) Å and c = 17.091(3) Å as determined by the Rietveld method).

2.2. Preparation of Mg-Doped $CuCrO_2$ Thin Films

In order to deposit $CuCrO_2$:Mg thin films, the target assembly was attached to an Alcatel A450 RF magnetron sputtering chamber (Alcatel, France). Fifteen minutes of pre-sputtering with argon plasma has been applied before starting the film deposition to remove the surface contamination. Pre-cleaned fused silica substrates (25 mm × 25 mm, ≃1 mm thick) placed on a water-cooled sample holder were used during the deposition. In order to avoid the reduction of the target, a low argon pressure [86] was used during the sputtering process. The deposition parameters are summarized in the Table 1. Under these conditions, as-deposited films with normalized thickness of 300 nm were elaborated. The X-ray fluorescence (XRF) measurement (not shown here) carried out with a Bruker S2 apparatus showed that the ratio was close to 1 Cu for 1 Cr in the film (with accuracy range of 5%) which is consistent with the composition of the target ($CuCr_{0.97}Mg_{0.03}O_2$).

The as-deposed films have been systematically annealed for 4 h under primary vacuum at various temperatures ranging from 450 to 650 °C.

Table 1. Process parameters for the deposition of delafossite Mg-doped $CuCrO_2$ by RF-sputtering.

Target material	3 at % Mg-doped $CuCrO_2$
Substrate	Fused quartz
Power ($W \cdot cm^{-2}$)	0.9
Magnetron	Yes
Argon pressure P (Pa)	0.5
Target to substrate distance d (cm)	5

2.3. Characterization

The structural properties of the films were investigated by a $\alpha = 1°$ grazing incidence X-ray diffraction (GIXRD) at room temperature. GIXRD was performed using a Siemens D5000 diffractometer equipped with a Bruker Sol-X detector (Siemens, Pittsburgh, PA, USA). Copper radiations were used as X-ray source ($\lambda CuK_{\alpha 1}$ = 1.5405 Å and $\lambda CuK_{\alpha 2}$ = 1.5445 Å). The microstructure of the films was observed using a Nanoscope III Dimension 3000 Atomic Force Microscope (AFM). AFM surface views were analyzed using the Gwyddion software. The band gap energy has been determined by the measure of the total transmittance and the total reflectance in the 300 to 1100 nm wavelength range using a Bentham PVE300 integrated spectrophotometer (Bentham Instruments Ltd., Berkshire, UK).

The electrical resistivity was measured using a four-point probe measurement unit (Signatone, Gilroy, CA, USA).

A home-made measurement setup has been used for the Seebeck coefficient determination as a function of temperature (Figure 1). Two independent heaters fitted to the thin film geometry have been used to apply a thermal gradient along the thin film. Electrical contacts were done with a 25 μm diameter aluminum wire bonder (HYBOND Model 626, Hybond, Escondido, CA, USA). The ohmic type behavior (linearity of current vs. voltage curve) of the electrical contacts has been checked systematically for all samples with a source meter (Keithley 2450, Tektronix, Beaverton, OR, USA) after bonding step. During the experiment, the voltage was measured with a nanovoltmeter (Keithley 2182A, Tektronix, Beaverton, OR, USA). Two carbon spots (emissivity coefficient of 0.97) were deposited on the surface of the thin films by spraying carbon solution through a shadow mask to accurately measure the surface temperature with an infrared camera. The two carbon spots were located at the same isotherm position than the electrical contacts. The mean temperature (T_{Mean}) was considered as the average between the temperature of the hot side (T_{Hot}) and that of the cold side (T_{Cold}).

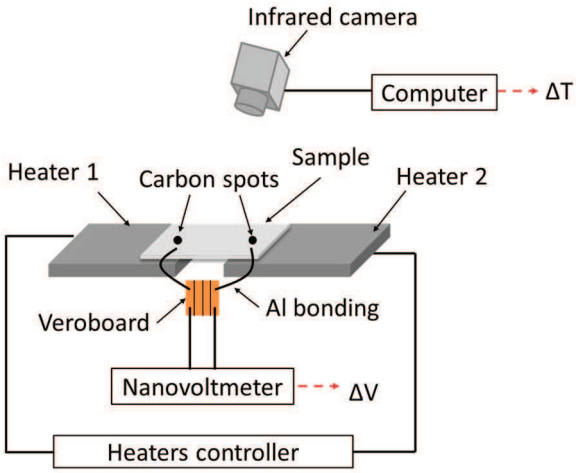

Figure 1. Seebeck coefficient measurement setup.

The Seebeck coefficient $S(T_{\text{Mean}})$ at a given mean temperature can be calculated with

$$S(T_{\text{Mean}}) = S_{\text{ref}} - \frac{\Delta V}{\Delta T} \tag{2}$$

where S_{ref}, ΔV, and ΔT are respectively Seebeck coefficient of the reference (Aluminum probe: S = 3.5 μV·K^{-1}), electric potential and temperature difference ($T_{\text{Hot}} - T_{\text{Cold}}$) measured on the film. The accuracy of the experimental setup was checked by using a bar of $Ca_3Co_4O_9$ already measured elsewhere with a ZEM3 commercial apparatus. The results were similar with a standard deviation of 7%.

3. Results and Discussion

3.1. Structural and Microstructural Characterizations

The GIXRD patterns of $CuCrO_2$:Mg thin films annealed for 4 h at various temperature in the 450 to 650 °C temperature range under primary vacuum have been measured for all samples. The as-deposited sample and the sample annealed at 450 °C were amorphous or nanocrystallized. The samples annealed above 500 °C corresponded to the target pattern of $CuCrO_2$ verifying the rhombohedral R-3m space group [87] (Figure 2). The full width at half maximum (FWHM) for the peak (012) decreased strongly with increasing annealing temperature (*AT*), up to 550 °C. For *AT* above 550 °C, the FWHM value was stable. As the instrumental contribution and the micro-strain are constant or negligible, it means that grain growth mainly occurred between 450 and 550 °C. The GIXRD pattern of the sample annealed at 450 and 550 °C were shown as an example in the Figure 2. All the characteristic Bragg peaks of the 3R delafossite phase are reported (PC-PDF file #39-0247). It confirms that the experimental conditions used to elaborate the samples provided a pure $CuCrO_2$:Mg phase. The lattice parameters determined by profile matching with constant scale factor were a = 2.96(7) Å and c = 17.14(5) Å.

In order to check the stability of the delafossite phase during the various measurements in temperature, a GIXRD analysis was done after a thermal treatment at 240 °C under air atmosphere for all samples. The result (Figure 2) shows similar patterns before (dark color) and after the thermal treatment for thin film initially annealed at 450 and 550 °C (light color). Thus, there were no additional phases formed during the physical characterization in temperature from room temperature to 220 °C in air atmosphere.

The AFM analysis of the $CuCrO_2$:Mg annealed at 450, 550, and 650 °C reveals the microstructure of the thin films (Figure 3). They exhibit nanocrystallized surfaces. The results show a smooth surface

for the 450 °C and 550 °C annealed films and for 650 °C annealed film, the grains are well-defined. Hence, the AFM results are in perfect agreement with the GIXRD analysis.

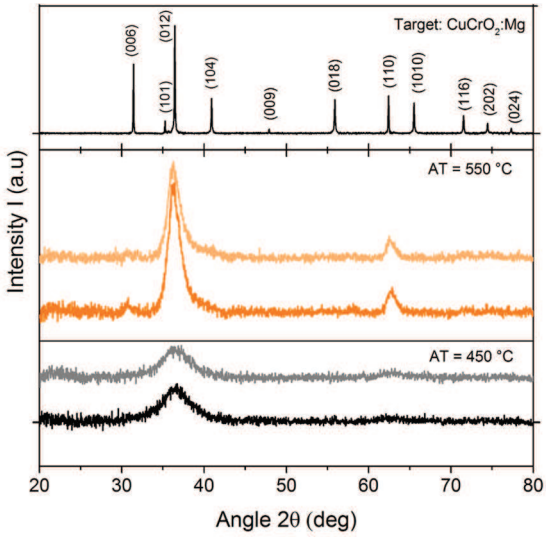

Figure 2. XRD pattern of the target, GIXRD patterns registered at room temperature (α = 1°) after annealing treatment (at 550 and 450 °C) (dark color) and GIXRD patterns of the same annealed samples registered after a thermal treatment at 240 °C under air atmosphere (light color).

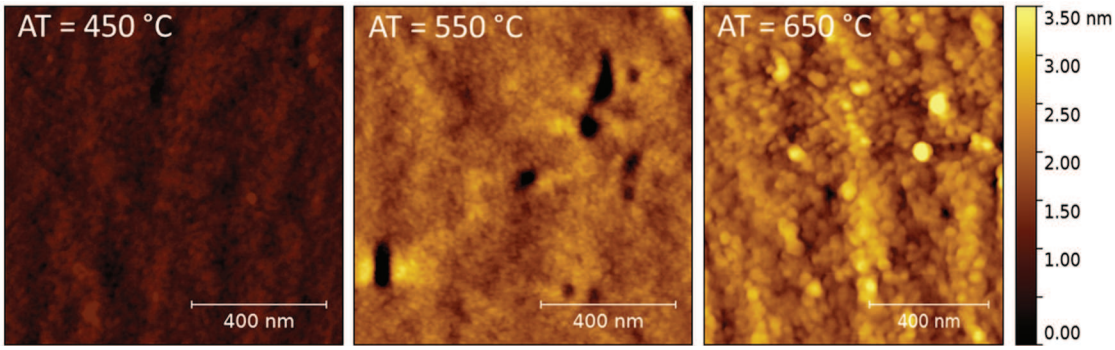

Figure 3. AFM micrographs of $CuCrO_2$:Mg thin films annealed at 450, 550, and 650 °C for 4 h under primary vacuum.

3.2. Transport Properties

The inset of the Figure 4a shows the electrical conductivity σ, at three measuring temperatures, of the 300 nm thick films as a function of the annealing temperature (*AT*). The as-deposited sample had the lowest electrical conductivity (at room temperature $\sigma_{\text{as-deposited}}$ = 6.10^{-3} S·cm^{-1}). This electrical conductivity measured at room temperature increased with the annealing temperature from 450 to 550 °C and reached 0.51 S·cm^{-1} then decreased slightly for higher annealing temperatures. Similar decrease of the electrical conductivity has already been observed by various authors and attributed to the decrease of copper vacancies and oxygen interstitials at higher temperatures [75,88] or microstructural changes [16]. In the literature, the electrical conductivity of $CuCrO_2$:Mg films ranged from 0.033 to 1.6 S·cm^{-1} [16,78,83,84,89,90]. For 305 nm thick $CuCrO_2$:Mg films, Rastogi et al. [84] found 0.1–0.2 S·cm^{-1} whereas, higher electrical conductivity of 0.6–1 S·cm^{-1} was obtained for 155 nm thick films. Their results are consistent with the present study.

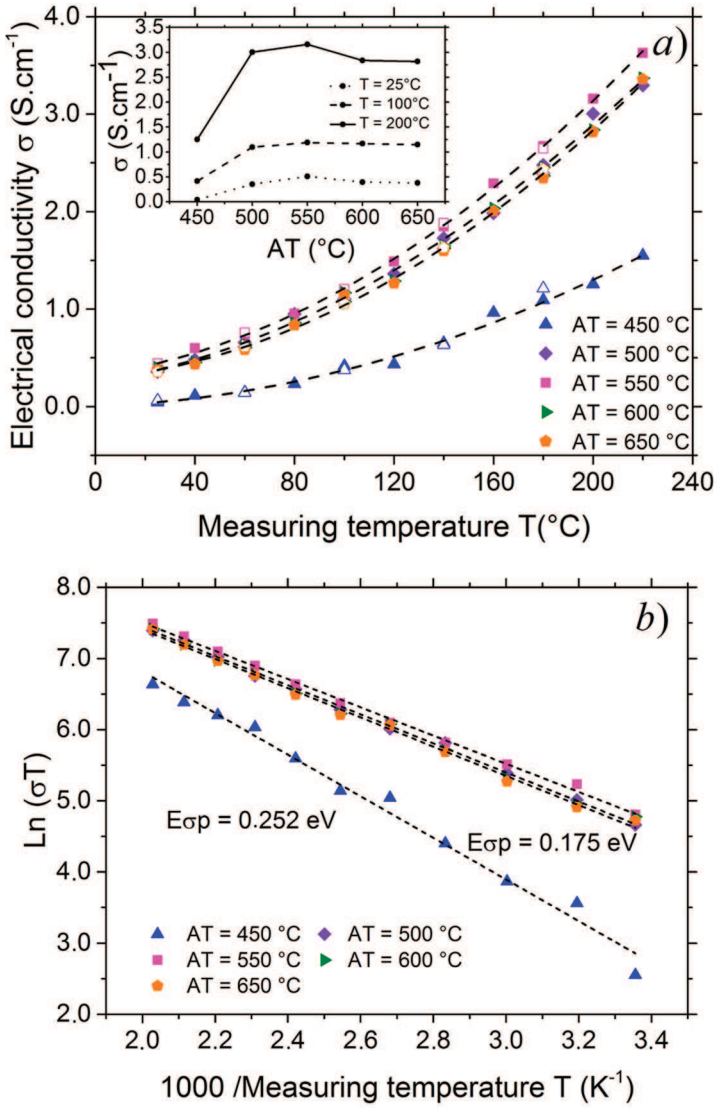

Figure 4. (**a**) Electrical conductivity σ of the films as a function of the measuring temperature *T* while heating (filled symbol) and cooling (empty symbol). Inset: Electrical conductivity *σ* of the films as a function of annealing temperatures (*AT*) at three different measuring temperatures; (**b**) Arrhenius plot of the electrical conductivity *σ*.

The Figure 4a,b shows the variation of the electrical conductivity of the $CuCrO_2$:Mg films with the measuring temperature. The electrical measurements showed that the variation of the electrical conductivity was fully reversible and increased with temperature as with semiconducting oxides.

For a semiconductor, the relation of the electrical conductivity with the temperature can be written in two ways considering that thermal energy is enough to activate the carriers (corresponding to the classical conduction mode) or not (corresponding to the hopping mechanism). In the second case, the thermal energy activates the small polarons and σ can be expressed as Equation (3). $CuCrO_2$ is known as a polaronic material where the transport mechanism is limited by small polaron hopping (SPH) [72,91–94].

In the case of small polarons, the expression of electrical conductivity is given by Mott and Davis [95]

$$\sigma = \frac{A_{\sigma p}}{T} e^{-\frac{E_{\sigma p}}{k_B T}} \quad (3)$$

where $A_{\sigma p}$ is a constant, $E_{\sigma p}$ is the activation energy of polaronic conduction.

In order to calculate the activation energy $E_{\sigma p}$ using SPH model, we plotted $\ln(\sigma T)$ versus $1000/T$ in the Figure 4b. The results showed a linear variation and the slope of the lines gave $E_{\sigma p}/k_B$. It is found that the polaronic activation energy decreased when annealing was carried out above 500 °C and reached a quasi-constant value close to 175 meV.

3.3. Seebeck Coefficient Measurement

The Figure 5a shows the Seebeck coefficient of the films as a function of the measuring temperature. The positive values of Seebeck coefficient confirmed that the $CuCrO_2$:Mg films were p-type semiconductors for all annealing temperatures. The lowest Seebeck coefficient was obtained for the highest electrical conductivity due to the carrier density variation. The measurement temperature, from 40 to 220 °C, did not influence the Seebeck coefficient. In the literature, the Seebeck coefficient of $CuCrO_2$:Mg bulk is ranging between 200–500 $\mu V \cdot K^{-1}$ and does not vary a lot with temperature in the 77 to 827 °C range [69,70,79] which is coherent with the present Seebeck measurements. Tripathi et al. [82] reported comparable value ($\simeq$+300 $\mu V \cdot K^{-1}$ at room temperature) for undoped $CuCrO_2$ films. On the other hand, Chikoidze et al. [83] published three times lower value of Seebeck coefficient (+130 $\mu V \cdot K^{-1}$ at 23 °C) for 4% Mg doped $CuCrO_2$ thin film. Overall, trends are similar and the difference in values could be explained by the difference in the measurement setup and the material type.

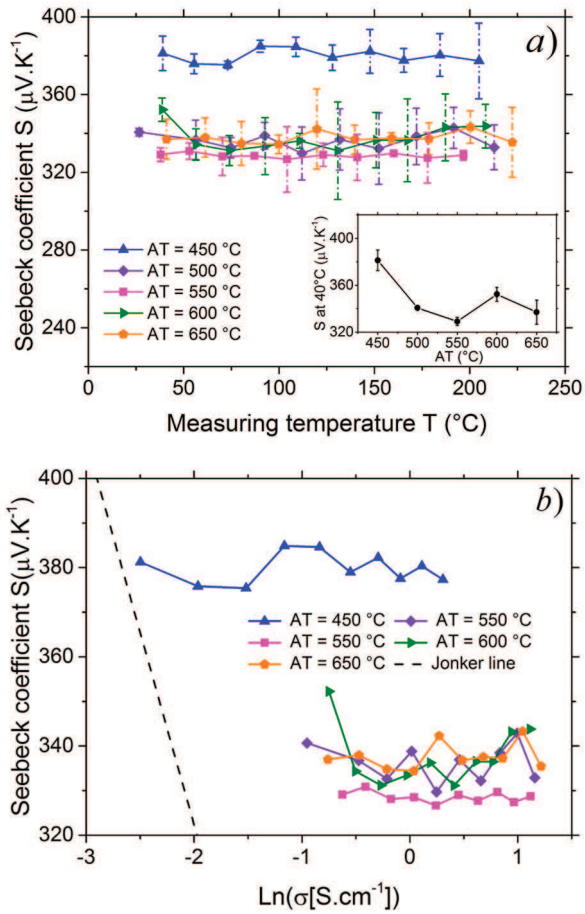

Figure 5. (**a**) Seebeck coefficient, *S*, of the films annealed at different temperatures as a function of the measuring temperature, *T*. Inset: Seebeck coefficient, *S*, of the films at 40 °C as a function of the annealing temperature, *AT*; (**b**) Jonker plot: the relationship of the Seebeck coefficient, *S*, to the electrical conductivity σ for different annealing temperatures, *AT*.

The invariance of Seebeck coefficient in temperature indicates that the hole density is constant between 40 and 220 °C. Therefore, the increase in electrical conductivity is the consequence of the increase in small polarons mobilities due to the hopping mechanism. In the classical conduction mode within the saturation regime, the electrical conductivity would have decreased because of the carrier mobility diminution ($\mu \propto T^{\frac{-3}{2}}$).

Jonker relation (Equation (4)) shows that Jonker plot S versus $\ln(\sigma)$ would have a slope $k_B/q = \pm 86.17$ μV·K^{-1} indicating the thermally activated non-degenerate semiconductor behavior (free carrier).

$$S = \pm \frac{k_B}{q}(\ln \sigma - \ln \sigma_0) \tag{4}$$

The plotted curves of the films in the inset of the Figure 5b were far away from the Jonker line. Consequently the Jonker plot S versus $\ln(\sigma)$ [96] showed a degenerate semiconductor behavior for the whole samples. Chikoidze et al. [83] noticed the quasi invariance of the Seebeck coefficient with the measurement temperature, which is consistent with the present results. Farrell et al. [72] also reported degenerate behavior for Cu deficient $CuCrO_2$ film.

3.4. Power Factor (PF)

The *PF* values were calculated from the electrical conductivity and the Seebeck coefficient ($PF = \sigma S^2$). The Figure 6a shows the variation of the *PF* at 40 °C as a function of the annealing temperature and the highest *PF* is obtained for samples annealed between 550 and 600 °C. The Figure 6b shows the power factor (*PF*) for the $CuCrO_2$:Mg films annealed at different temperatures, as a function of the measuring temperature and gives a comparison with the data from the literature. As the Seebeck coefficient was quasi constant with increasing temperature, the *PF* followed the electrical conductivity variation. It increased with increasing measurement temperature. Around 220 °C, it reached 38 μW·m^{-1}·K^{-2}. $CuCrO_2$:Mg films had a higher *PF* than the $CuCrO_2$ bulk studied by Ruttanapun et al. [80]. However, their *PF* were lower than the experimentally achieved *PF* of $CuCrO_2$:Mg bulk materials [69]. For example, Q. Meng et al. found 65 μW·m^{-1}·K^{-2} at 40 °C for $CuCrO_2$:Mg bulk material [79] thanks to the high electrical conductivity. In comparison with the *PF* obtained with bulk material, a slight improvement of the power factor of $CuCrO_2$:Mg in the form of thin film could still be achieved by optimizing the film nanostructuration. Moreover, the thickness of the films deposited by RF-magnetron sputtering were 300 nm and showed columnar nanometric grains [16] which implies a lower thermal conductivity due to phonon boundary scattering without reducing the electrical conductivity.

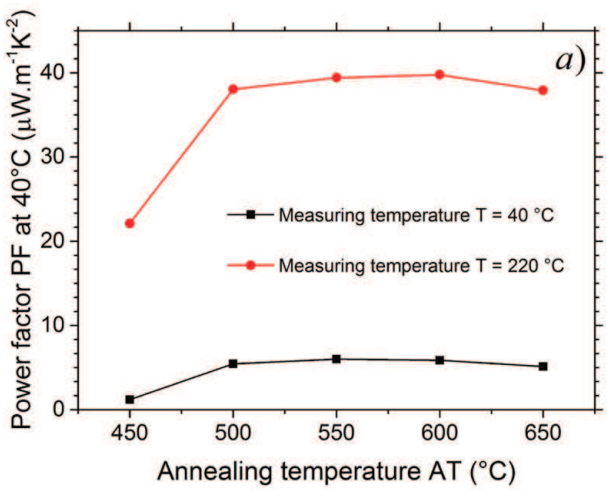

Figure 6. *Cont.*

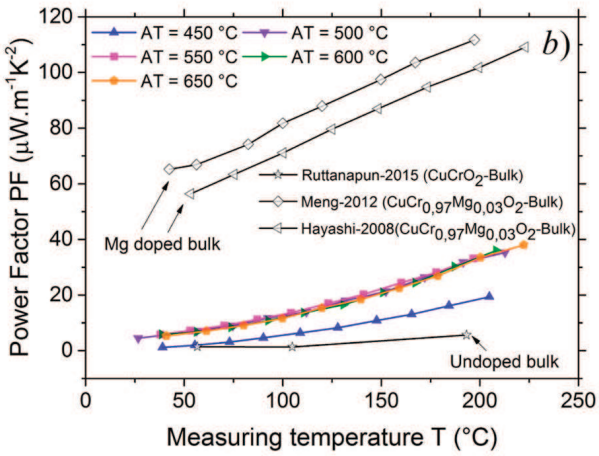

Figure 6. (**a**) Power factor *PF* at 40 and 220 °C as a function of the annealing temperature *AT*; (**b**) Power factor *PF* of annealed thin films as a function of the measuring temperature *T* and comparison with the data from the literature.

The main advantage of the thin film compared to the bulk is noticeable with the figure of merit *ZT* where the thermal conductivity is taken into account. Indeed, the lattice thermal conductivity in thin films is generally lower than the bulk materials [2,7,8]. However, in this work, the values for *ZT* have not been calculated because the thermal conductivity of $CuCrO_2$:Mg in the form of thin films could not be measured.

3.5. Optoelectrical Properties and Fermi Energy Level

The fundamental indirect band gap energy was determined by the measurements of the total transmittance *TT* (specular and diffuse) and the total reflectance *TR* (not shown here). The Tauc's plot [97] gives the optical fundamental band gap from the linear extrapolation of the curve slope to intercept the energy axis (Figure 7). In detail, the absorption coefficient α, was estimated from the relation [98]

$$\alpha = \frac{1}{d} \ln\left(\frac{(1-TR)^2}{TT}\right) \tag{5}$$

where d is the film thickness. The fundamental indirect band gap energy was determined using the absorption coefficient α via the relation

$$(\alpha h\upsilon)^m = A(h\upsilon - E_g) \tag{6}$$

where $h\nu$ is the photon energy, E_g is the optical band gap, A is a constant called the band tailing parameter and $m = 1/2$ for the fundamental indirect transition. Using the Tauc's method, 2.73 eV was obtained for the fundamental indirect transition (Figure 7). The obtained energy value is consistent with the literature [84] and shows a wide band gap which avoids the simultaneous presence of the electron and hole in their specific bands and drives to a high Seebeck coefficient even at high temperatures. A similar indirect band gap value was obtained by Chikoidze et al. [83] and Kaya et al. [99].

The Fermi energy was calculated using the following Mott formula [100] for a degenerate electron gas approximation

$$S \approx -\frac{\pi^2 k_B^2 T}{3qE_F} \tag{7}$$

In this case, the Fermi energy is taken from the valence band edge. At 40 °C, the Fermi energy value was 0.022 ± 0.002 eV which is lower than the thermal energy ($3k_BT$ = 0.081 eV at 314 K) on the Fermi distribution width. It leads to the conclusion that the samples did not display thermally

activated characteristics, which is consistent for a degenerate semiconductor. The Fermi level can trace the work function of the delafossite and give precious information about which metal can be used for ohmic contact (to avoid the Schottky barriers) with the delafossite. This information is needed for the thermoelectric, optoelectronic, and photocatalytic applications.

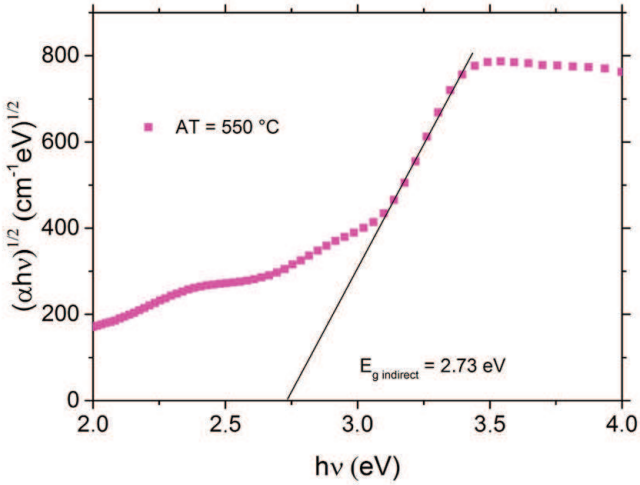

Figure 7. $(\alpha h\nu)^{1/2}$ vs. hν plot for the fundamental indirect optical band gap energy analysis.

3.6. Carrier Concentration and Hole Effective Mass

According to the Hubbard model [101] and Heike's formula [102] adapted for degenerate semiconductor with a carrier hopping mechanism, the Seebeck coefficient can be written as Equation (8)

$$S = +\frac{k_B}{q}\left[\left(\frac{g_1}{g_2}\right)\frac{[Cu^+]}{[Cu^{2+}]}\right] \tag{8}$$

where g is the spin and orbital degeneracy and $[Cu^+]/[Cu^{2+}]$ is the ratio of the ion concentrations.

At high temperature, due to the mixed valences of the copper (Cu^+/Cu^{2+}) in the $CuCrO_2$:Mg, the Seebeck coefficient which is the measure of the entropy of the carriers is given by the spin and orbital degeneracy [73]. The Figure 8 shows the spin and orbital degeneracies of Cu^+ (g_1) and Cu^{2+} (g_2) due to Mg^{2+} doping compensation according to $(Cu^{+}{}_{1-x}Cu^{2+}{}_{x})(Cr^{3+}{}_{1-x}Mg^{2+}{}_{x})O_2$ in the linear bonding O–Cu–O (where the coordination number of Cu is 2). Thereby, from the measured Seebeck coefficient, the concentration of Cu^+ and Cu^{2+} ions have been estimated and they varied barely with the annealing temperature (*AT*). The obtained values were $[Cu^+] = 0.995$ and $[Cu^{2+}] = 0.005$ for *AT* above 500 °C.

Using the unit cell volumes determined by the GIXRD measurements, the density of total copper site d_{Cu} in the delafossite structure is estimated at $(2.30 \pm 0.02) \times 10^{22}$ cm^{-3}. The hole density which is related to the Cu^{2+} concentration is equal to $d_{Cu} \times [Cu^{2+}] = (1.17 \pm 0.05) \times 10^{20}$ cm^{-3}.

The hole effective mass, m^*, was calculated using the equation

$$m^* = \frac{\hbar^2}{2E_F}(3\pi^2 h_s)^{2/3} \tag{9}$$

where $\hbar$ is the reduced Planck constant and h_s is the hole density.

The hole effective mass estimated for $CuCrO_2$:Mg was $3.80 \pm 0.2\ m_0$ which is close to the effective mass predicted theoretically for $CuCrO_2$ by Scanlon et al. [103] (without spin-orbit coupling $m^*_{th} = 2.96\ m_0$ and with spin-orbit coupling $m^*_{th} = 4.53\ m_0$).

The effective hole mass is rarely published for this type of material. However, it is requisite for the optoelectronic application in particular for the determination of the hole mobility.

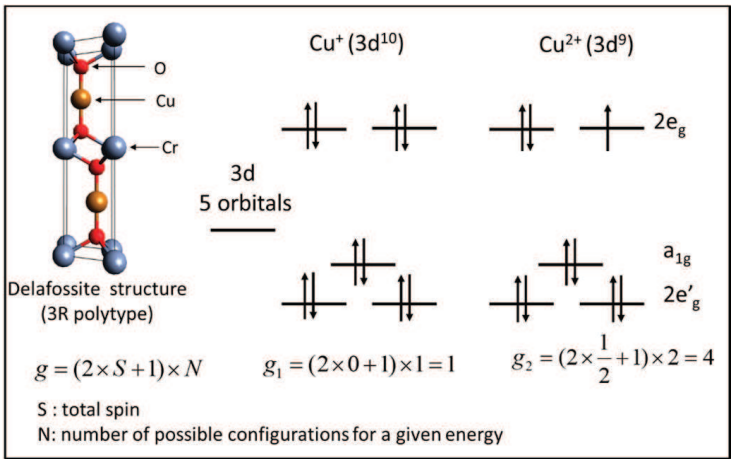

Figure 8. Spin and orbital degeneracies of Cu^{+} and Cu^{2+} in the delafossite structure.

4. Conclusions

$CuCrO_2$:Mg thin films have been elaborated by RF magnetron sputtering and annealed at different temperatures between 450 and 650 °C under primary vacuum. The as-deposited film and the film annealed at 450 °C were nanocrystalized, whereas the films annealed above 500 °C had a delafossite structure. The AFM has shown a nanometric grains sizes and smooth surface at the optimal annealing temperature. The higher electrical conductivity determined at 40 °C was 0.60 $S \cdot cm^{-1}$ for the film annealed at 550 °C which had a Seebeck coefficient of +329 $\mu V \cdot K^{-1}$. We analyzed the small polaron hopping conductivity mechanism and found a degenerate semiconductor behavior of the $CuCrO_2$:Mg thin films. Thanks to its constant Seebeck coefficient between 40 and 220 °C and high fundamental indirect band gap energy, the power factor increased like the electrical conductivity when the temperature was increased, and reached 38 $\mu W \cdot m^{-1} \cdot K^{-2}$ at 220 °C. $CuCrO_2$:Mg thin films have been studied for their TE properties and showed encouraging results. Their high and constant Seebeck coefficient in changing temperatures and their stability in air atmosphere could be a great advantage for an application of this material in high accuracy temperature measurement devices, miniaturized devices in thin film configuration, and also transparent TE devices due to its TCO properties.

Acknowledgments: The authors would like to thank the French ministry of Research for the National PhD funding.

Author Contributions: I. Sinnarasa has deposited and characterized the thin films and wrote the paper. Y. Thimont is the coordinated of this research work, he processed and analyzed the TE properties and developed the TE measurement setup devoted to the thin films geometry, he has contributed to the paper writing. L. Presmanes has contributed to the sputtering parameters optimization and the nanostructuration characterization. A. Barnabé and P. Tailhades have characterized the structure of the delafossite thin films.

Conflicts of Interest: The authors declare no conflict of interest.

References

1. Rowe, D.M. *CRC Handbook of Thermoelectrics*; CRC Press: Boca Raton, FL, USA, 1995.
2. Alam, H.; Ramakrishna, S. A review on the enhancement of figure of merit from bulk to nano-thermoelectric materials. *Nano Energy* **2013**, *2*, 190–212. [CrossRef]
3. Martin, J.; Tritt, T.; Uher, C. High temperature Seebeck coefficient metrology. *J. Appl. Phys.* **2010**, *108*, 121101. [CrossRef]
4. Aswal, D.K.; Basu, R.; Singh, A. Key issues in development of thermoelectric power generators: High figure-of-merit materials and their highly conducting interfaces with metallic interconnects. *Energy Convers. Manag.* **2016**, *114*, 50–67. [CrossRef]

5. Dresselhaus, M.S.; Chen, G.; Tang, M.Y.; Yang, R.G.; Lee, H.; Wang, D.Z.; Ren, Z.F.; Fleurial, J.-P.; Gogna, P. New Directions for Low-Dimensional Thermoelectric Materials. *Adv. Mater.* **2007**, *19*, 1043–1053. [CrossRef]
6. Chen, Z.-G.; Han, G.; Yang, L.; Cheng, L.; Zou, J. Nanostructured thermoelectric materials: Current research and future challenge. *Prog. Nat. Sci. Mater. Int.* **2012**, *22*, 535–549. [CrossRef]
7. Cahill, D.G.; Fischer, H.E.; Klitsner, T.; Swartz, E.T.; Pohl, R.O. Thermal conductivity of thin films: Measurements and understanding. *J. Vac. Sci. Technol. A Vac. Surf. Films* **1989**, *7*, 1259–1266. [CrossRef]
8. Loureiro, J.; Santos, J.R.; Nogueira, A.; Wyczisk, F.; Divay, L.; Reparaz, S.; Alzina, F.; Sotomayor Torres, C.M.; Cuffe, J.; Montemor, F.; et al. Nanostructured p-type Cr/V_2O_5 thin films with boosted thermoelectric properties. *J. Mater. Chem. A* **2014**, *2*, 6456–6462. [CrossRef]
9. Venkatasubramanian, R.; Siivola, E.; O'Quinn, B.; Coonley, K.; Colpitts, T.; Addepalli, P.; Napier, M.; Mantini, M. Nanostructured Superlattice Thin-Film Thermoelectric Devices. In *Nanotechnology and the Environment*; ACS Symposium Series; American Chemical Society: Washington, DC, USA, 2004; pp. 347–352.
10. Benko, F.A.A.; Koffyberg, F.P.P. Preparation and opto-electronic properties of semi-conducting $CuCrO_2$. *Mater. Res. Bull.* **1986**, *21*, 753–757. [CrossRef]
11. Kawazoe, H.; Yasukawa, M.; Hyodo, H.; Kurita, M.; Yanagi, H.; Hosono, H. p-type electrical conduction in transparent thin films of $CuAlO_2$. *Nature* **1997**, *389*, 939–942. [CrossRef]
12. Nagarajan, R.; Duan, N.; Jayaraj, M.K.; Li, J.; Vanaja, K.A.; Yokochi, A.; Draeseke, A.; Tate, J.; Sleight, A.W. p-Type conductivity in the delafossite structure. *Int. J. Inorg. Mater.* **2001**, *3*, 265–270. [CrossRef]
13. Yanagi, H.; Hase, T.; Ibuki, S.; Ueda, K.; Hosono, H. Bipolarity in electrical conduction of transparent oxide semiconductor $CuInO_2$ with delafossite structure. *Appl. Phys. Lett.* **2001**, *78*, 1583–1585. [CrossRef]
14. Banerjee, A.N.; Chattopadhyay, K.K. Recent developments in the emerging field of crystalline p-type transparent conducting oxide thin films. *Prog. Cryst. Growth Charact. Mater.* **2005**, *50*, 52–105. [CrossRef]
15. Stadler, A. Transparent Conducting Oxides-An Up-To-Date Overview. *Materials* **2012**, *5*, 661–683. [CrossRef]
16. Barnabé, A.; Thimont, Y.; Lalanne, M.; Presmanes, L.; Tailhades, P. *P*-type conducting transparent characteristics of delafossite Mg-doped $CuCrO_2$ thin films preparation by RF-sputtering. *J. Mater. Chem. C* **2015**, *3*, 6012–6024. [CrossRef]
17. Zhang, K.H.L.; Xi, K.; Blamire, M.G.; Egdell, R.G. *P*-type transparent conducting oxides. *J. Phys. Condens. Matter* **2016**, *28*, 383002. [CrossRef] [PubMed]
18. Barquinha, P.; Martins, R.; Pereira, L.; Fortunato, E. *Transparent Oxide Electronics: From Materials to Devices*; John Wiley & Sons, Ltd.: Hoboken, NJ, USA, 2008.
19. Wager, J.F.; Kesler, D.A.; Presley, D.A. *Transparent Electronics*; Springer: New York, NY, USA, 2008.
20. Tonooka, K.; Kikuchi, N. Preparation of transparent $CuCrO_2$: Mg/ZnO p-n junctions by pulsed laser deposition. *Thin Solid Films* **2006**, *515*, 2415–2418. [CrossRef]
21. Hosono, H.; Ota, H.; Kawamura, K.; Sarukura, N.; Hirano, M. Light-Emitting Diode and Laser Diode Having *N*-Type ZnO Layer and *P*-Type Semiconductor Laser. U.S. Patent 6,806,503, 19 October 2004.
22. Yanagi, H.; Ueda, K.; Ohta, H.; Orita, M.; Hirano, M.; Hosono, H. Fabrication of all oxide transparent *p-n* homojunction using bipolar $CuInO_2$ semiconducting oxide with delafossite structure. *Solid State Commun.* **2002**, *121*, 15–18. [CrossRef]
23. Ling, B.; Zhao, J.L.; Sun, X.W.; Tan, S.T.; Kyaw, A.K.K.; Divayana, Y.; Dong, Z.L. Color tunable light-emitting diodes based on p+-Si/p-$CuAlO_2$ /n-ZnO nanorod array heterojunctions. *Appl. Phys. Lett.* **2010**, *97*, 13101. [CrossRef]
24. Chiu, T.W.; Tonooka, K.; Kikuchi, N. Fabrication of ZnO and $CuCrO_2$: Mg thin films by pulsed laser deposition with in situ laser annealing and its application to oxide diodes. *Thin Solid Films* **2008**, *516*, 5941–5947. [CrossRef]
25. Tate, J.; Jayaraj, M.K.K.; Draeseke, A.D.D.; Ulbrich, T.; Sleight, A.W.W.; Vanaja, K.A.; Nagarajan, R.; Wager, J.F.F.; Hoffman, R.L.L. p-Type oxides for use in transparent diodes. *Thin Solid Films* **2002**, *411*, 119–124. [CrossRef]
26. Renaud, A.; Cario, L.; Deniard, P.; Gautron, E.; Rocquefelte, X.; Pellegrin, Y.; Blart, E.; Odobel, F.; Jobic, S. Impact of Mg Doping on Performances of $CuGaO_2$ Based p-Type Dye-Sensitized Solar Cells. *J. Phys. Chem. C* **2014**, *118*, 54–59. [CrossRef]
27. Asemi, M.; Ghanaatshoar, M. Hydrothermal growth of one-dimensional Ce-doped TiO_2 nanostructures for solid-state DSSCs comprising Mg-doped $CuCrO_2$. *J. Mater. Sci.* **2017**, *52*, 489–503. [CrossRef]

28. Zhu, T.; Deng, Z.; Fang, X.; Huo, Z.; Wang, S.; Dong, W.; Shao, J.; Tao, R.; Song, C.; Wang, L. High photovoltages of $CuFeO_2$ based p-type dye-sensitized solar cells. *J. Alloys Compd.* **2016**, *685*, 836–840. [CrossRef]
29. Jiang, T.; Bujoli-Doeuff, M.; Farré, Y.; Blart, E.; Pellegrin, Y.; Gautron, E.; Boujtita, M.; Cario, L.; Odobel, F.; Jobic, S. Copper borate as a photocathode in p-type dye-sensitized solar cells. *RSC Adv.* **2016**, *6*, 1549–1553. [CrossRef]
30. Wuttig, A.; Krizan, J.W.; Gu, J.; Frick, J.J.; Cava, R.J.; Bocarsly, A.B. The effect of Mg-doping and Cu nonstoichiometry on the photoelectrochemical response of $CuFeO_2$. *J. Mater. Chem. A* **2017**, *5*, 165–171. [CrossRef]
31. Toyoda, K.; Hinogami, R.; Miyata, N.; Aizawa, M. Calculated Descriptors of Catalytic Activity for Water Electrolysis Anode: Application to Delafossite Oxides. *J. Phys. Chem. C* **2015**, *119*, 6495–6501. [CrossRef]
32. Carcia, P.F.; Shannon, R.D.; Bierstedt, P.E.; Flippen, R.B. Oxygen electrocatalysis on Thin Film Metallic Oxide Electrodes with the Delafossite Structure. *J. Electrochem. Soc.* **1980**, *127*, 1974. [CrossRef]
33. Dong, H.; Li, Z.; Xu, X.; Ding, Z.; Wu, L.; Wang, X.; Fu, X. Visible light-induced photocatalytic activity of delafossite $AgMO_2$ (M=Al, Ga, In) prepared via a hydrothermal method. *Appl. Catal. B Environ.* **2009**, *89*, 551–556. [CrossRef]
34. Ketir, W.; Rekhila, G.; Trari, M.; Amrane, A. Preparation, characterization and application of $CuCrO_2$/ZnO photocatalysts for the reduction of Cr(VI). *J. Environ. Sci.* **2012**, *24*, 2173–2179. [CrossRef]
35. Saadi, S.; Bouguelia, A.; Trari, M. Photocatalytic hydrogen evolution over $CuCrO_2$. *Sol. Energy* **2006**, *80*, 272–280. [CrossRef]
36. Rao, R.; Dandekar, A.; Baker, R.T.K.; Vannice, M.A. Properties of Copper Chromite Catalysts in Hydrogenation Reactions. *J. Catal.* **1997**, *171*, 406–419. [CrossRef]
37. Koriche, N.; Bouguelia, A.; Aider, A.; Trari, M. Photocatalytic hydrogen evolution over delafossite. *Int. J. Hydrog. Energy* **2005**, *30*, 693–699. [CrossRef]
38. Ketir, W.; Bouguelia, A.; Trari, M. Visible Light Induced NO_2 (-) Removal Over $CuCrO_2$ Catalyst. *Water Air Soil Pollut.* **2009**, *199*, 115–122. [CrossRef]
39. Zhang, P.; Shi, Y.; Chi, M.; Park, J.N.; Stucky, G.D.; McFarland, E.W.; Gao, L. Mesoporous delafossite $CuCrO_2$ and spinel $CuCr_2O_4$: Synthesis and catalysis. *Nanotechnology* **2013**, *24*, 345704. [CrossRef] [PubMed]
40. Jang, Y.J.; Park, Y.B.; Kim, H.E.; Choi, Y.H.; Choi, S.H.; Lee, J.S. Oxygen-Intercalated $CuFeO_2$ Photocathode Fabricated by Hybrid Microwave Annealing for Efficient Solar Hydrogen Production. *Chem. Mater.* **2016**, *28*, 6054–6061. [CrossRef]
41. Lekse, J.W.; Underwood, M.K.; Lewis, J.P.; Matranga, C. Synthesis, Characterization, Electronic Structure, and Photocatalytic Behavior of $CuGaO_2$ and $CuGa_{1-x}Fe_xO_2$(x = 0.05, 0.10, 0.15, 0.20) Delafossites. *J. Phys. Chem. C* **2012**, *116*, 1865–1872. [CrossRef]
42. Chiu, T.W.; Yang, Y.C.; Yeh, A.C.; Wang, Y.P.; Feng, Y.W. Antibacterial property of $CuCrO_2$ thin films prepared by RF magnetron sputtering deposition. *Vacuum* **2013**, *87*, 174–177. [CrossRef]
43. Doumerc, J.P.; Parent, C.; Chao, Z.J.; Le Flem, G.; Ammar, A. Luminescence of the Cu^+ ion in $CuLaO_2$. *J. Less Common Met.* **1989**, *148*, 333–337. [CrossRef]
44. Jacob, A.; Parent, C.; Boutinaud, C.; Le Flem, G.; Doumerc, J.P.; Ammar, A.; Elazhari, M.; Elaatmani, M. Luminescent properties of Delafossite-type oxides $LaCuO_2$ and $YCuO_2$. *Solid State Commun.* **1997**, *103*, 529–532. [CrossRef]
45. Byrne, D.; Cowley, A.; Bennett, N.; McGlynn, E. The luminescent properties of $CuAlO_2$. *J. Mater. Chem. C* **2014**, *2*, 7859–7868. [CrossRef]
46. Patzsch, J.; Balog, I.; Krauß, P.; Lehmann, C.W.; Schneider, J.J. Synthesis, characterization and p–n type gas sensing behaviour of $CuFeO_2$ delafossite type inorganic wires using Fe and Cu complexes as single source molecular precursors. *RSC Adv.* **2014**, *4*, 15348. [CrossRef]
47. Elgazzar, E.; Tataroğlu, A.; Al-Ghamdi, A.A.; Al-Turki, Y.; Farooq, W.A.; El-Tantawy, F.; Yakuphanoglu, F. Thermal sensors based on delafossite film/p-silicon diode for low-temperature measurements. *Appl. Phys. A* **2016**, *122*, 617. [CrossRef]
48. Zheng, X.G.; Taniguchi, K.; Takahashi, A.; Liu, Y.; Xu, C.N. Room temperature sensing of ozone by transparent p-type semiconductor $CuAlO_2$. *Appl. Phys. Lett.* **2004**, *85*, 1728–1729. [CrossRef]
49. Zhou, S.; Fang, X.; Deng, Z.; Li, D.; Dong, W.; Tao, R.; Meng, G.; Wang, T. Room temperature ozone sensing properties of p-type $CuCrO_2$ nanocrystals. *Sens. Actuators B* **2009**, *143*, 119–123. [CrossRef]

50. Uhrmacher, M.; Attili, R.N.; Lieb, K.P.; Winzer, K.; Mekata, M. Perturbed Angular Correlation Measurements in 2D Spin-Frustrated $CuFeO_2$. *Phys. Rev. Lett.* **1996**, *76*, 4829–4831. [CrossRef] [PubMed]
51. Terada, N.; Mitsuda, S.; Oohara, Y.; Yoshizawa, H.; Takei, H. Anomalous magnetic excitation on triangular lattice antiferromagnet $CuFeO_2$. *J. Magn. Magn. Mater.* **2004**, *272–276*, e997–e998. [CrossRef]
52. Hoffman, R.; Wager, J. Transistor Device Having a Delafossite Material. U.S. Patent 7,026,713, 11 April 2006.
53. Maignan, A.; Martin, C.; Frésard, R.; Eyert, V.; Guilmeau, E.; Hébert, S.; Poienar, M.; Pelloquin, D. On the strong impact of doping in the triangular antiferromagnet $CuCrO_2$. *Solid State Commun.* **2009**, *149*, 962–967. [CrossRef]
54. O'Sullivan, M.; Stamenov, P.; Alaria, J.; Venkatesan, M.; Coey, J.M.D. Magnetoresistance of $CuCrO_2$-based delafossite films. *J. Phys. Conf. Ser.* **2010**, *200*, 052021. [CrossRef]
55. Shu, J.; Zhu, X.; Yi, T. $CuCrO_2$ as anode material for lithium ion batteries. *Electrochim. Acta* **2009**, *54*, 2795–2799. [CrossRef]
56. Huang, X.; Ni, C.; Zhao, G.; Irvine, J.T.S. Oxygen storage capacity and thermal stability of the $CuMnO_2$–CeO_2 composite system. *J. Mater. Chem. A* **2015**, *3*, 12958–12964. [CrossRef]
57. Díaz-García, A.K.; Lana-Villarreal, T.; Gómez, R. Sol–gel copper chromium delafossite thin films as stable oxide photocathodes for water splitting. *J. Mater. Chem. A* **2015**, *3*, 19683–19687. [CrossRef]
58. Taddee, C.; Kamwanna, T.; Amornkitbamrung, V. Characterization of transparent superconductivity Fe-doped $CuCrO_2$ delafossite oxide. *Appl. Surf. Sci.* **2016**, *380*, 237–242. [CrossRef]
59. Suriwong, T.; Thongtem, T.; Thongtem, S. Thermoelectric and optical properties of $CuAlO_2$ synthesized by direct microwave heating. *Curr. Appl. Phys.* **2014**, *14*, 1257–1262. [CrossRef]
60. Hayashi, K.; Nozaki, T.; Kajitani, T. Structure and High Temperature Thermoelectric Properties of Delafossite-Type Oxide $CuFe_{1-x}Ni_xO_2$ ($0 \leq x \leq 0.05$). *Jpn. J. Appl. Phys.* **2007**, *46*, 5226–5229. [CrossRef]
61. Park, K.; Ko, K.Y.; Kwon, H.C.; Nahm, S. Improvement in thermoelectric properties of $CuAlO_2$ by adding Fe_2O_3. *J. Alloys Compd.* **2007**, *437*, 1–6. [CrossRef]
62. Isawa, K.; Yaegashi, Y.; Ogota, S.; Nagano, M.; Sudo, S.; Yamada, K.; Yamauchi, H. Thermoelectric power of delafossite-derived compounds, $RCuO_2 + \delta$ (R = Y, La, Pr, Nd, Sm, and Eu). *Phys. Rev. B* **1998**, *57*, 7950–7954. [CrossRef]
63. Banerjee, A.N.; Maity, R.; Ghosh, P.K.; Chattopadhyay, K.K. Thermoelectric properties and electrical characteristics of sputter-deposited P-$CuAlO_2$ thin films. *Thin Solid Films* **2005**, *474*, 261–266. [CrossRef]
64. Park, K.; Ko, K.Y.; Seo, W.-S. Thermoelectric properties of $CuAlO_2$. *J. Eur. Ceram. Soc.* **2005**, *25*, 2219–2222. [CrossRef]
65. Guilmeau, E.; Maignan, A.; Martin, C. Thermoelectric Oxides: Effect of Doping in Delafossites and Zinc Oxide. *J. Electron. Mater.* **2009**, *38*, 1104–1107. [CrossRef]
66. Nozaki, T.; Hayashi, K.; Kajitani, T.; Nozaki, K.; Hayashi, K.; Kajitani, T. Electronic Structure and Thermoelectric Properties of the Delafossite-Type Oxides $CuFe_{1-x}Ni_xO_2$. *J. Electron. Mater.* **2009**, *38*, 1282–1286. [CrossRef]
67. Ruttanapun, C. Effects of Pd substitution on the thermoelectric and electronic properties of delafossite $Cu_{1-x}Pd_xFeO_2$ (x = 0.01, 0.03 and 0.05). *J. Solid State Chem.* **2014**, *215*, 43–49. [CrossRef]
68. Powar, S.; Xiong, D.; Daeneke, T.; Ma, M.T.; Gupta, A.; Lee, G.; Makuta, S.; Tachibana, Y.; Chen, W.; Spiccia, L.; et al. Improved Photovoltages for p-Type Dye-Sensitized Solar Cells Using $CuCrO_2$ Nanoparticles. *J. Phys. Chem. C* **2014**, *118*, 16375–16379. [CrossRef]
69. Hayashi, K.; Sato, K.I.; Nozaki, K.; Kajitani, T. Effect of Doping on Thermoelectric Properties of Delafossite-Type Oxide $CuCrO_2$. *Jpn. J. Appl. Phys.* **2008**, *57*, 59–63. [CrossRef]
70. Ono, Y.; Satoh, K.; Nozaki, T.; Kajitani, T. Structural, Magnetic and Thermoelectric Properties of Delafossite-type Oxide, $CuCr_{1-x}Mg_xO_2$ ($0 \leq x \leq 0.05$). *Jpn. J. Appl. Phys* **2007**, *46*, 1071–1075. [CrossRef]
71. Okuda, T.; Jufuku, N.; Hidaka, S.; Terada, N. Magnetic, transport, and thermoelectric properties of the delafossite oxides $CuCr_{1-x}Mg_xO_2$ ($0 \leq x \leq 0.04$). *Phys. Rev. B* **2005**, *72*, 144403. [CrossRef]
72. Farrell, L.; Norton, E.; Smith, C.M.; Caffrey, D.; Shvets, I.V.; Fleischer, K. Synthesis of nanocrystalline Cu deficient $CuCrO_2$—A high figure of merit p-type transparent semiconductor. *J. Mater. Chem. C* **2016**, *126*, 126–134. [CrossRef]
73. Lunca Popa, P.; Crêpellière, J.; Leturcq, R.; Lenoble, D. Electrical and optical properties of Cu–Cr–O thin films fabricated by chemical vapour deposition. *Thin Solid Films* **2016**, *612*, 194–201. [CrossRef]

74. Ngo, T.N.M.; Palstra, T.T.M.; Blake, G.R. Crystallite size dependence of thermoelectric performance of $CuCrO_2$. *RSC Adv.* **2016**, *6*, 91171–91178. [CrossRef]
75. Gotzendorfer, S.; Bywalez, R.; Lobmann, P. Preparation of p-type conducting transparent $CuCrO_2$ and $CuAl_{0.5}Cr_{0.5}O_2$ thin films by sol-gel processing. *J. Sol-Gel Sci. Technol.* **2009**, *52*, 113–119. [CrossRef]
76. Lin, F.; Gao, C.; Zhou, X.; Shi, W.; Liu, A. Magnetic, electrical and optical properties of p-type Fe-doped $CuCrO_2$ semiconductor thin films. *J. Alloys Compd.* **2013**, *581*, 502–507. [CrossRef]
77. Yu, R.-S.; Hu, D.-H. Formation and characterization of p-type semiconductor $CuCrO_2$ thin films prepared by a sol–gel method. *Ceram. Int.* **2015**, *41*, 9383–9391. [CrossRef]
78. Chen, H.; Wu, J.; Huang, C. Development of a fast annealing process to prepare transparent conductive Mg-doped $CuCrO_2$ thin films. *Thin Solid Films* **2016**, *605*, 180–185. [CrossRef]
79. Meng, Q.; Lu, S.S.; Lu, S.S.; Xiang, Y. Preparation of p-type $CuCr_{1-x}Mg_xO_2$ bulk with improved thermoelectric properties by sol-gel method. *J. Sol-Gel Sci. Technol.* **2012**, *63*, 1–7. [CrossRef]
80. Ruttanapun, C.; Maensiri, S. Effects of spin entropy and lattice strain from mixed-trivalent Fe^{3+}/Cr^{3+} on the electronic, thermoelectric and optical properties of delafossite $CuFe_{1-x}Cr_xO_2$. *J. Phys. D Appl. Phys.* **2015**, *48*, 495103. [CrossRef]
81. Nagarajan, R.; Draeseke, A.D.; Sleight, A.W.; Tate, J. *P*-type conductivity in $CuCr_{1-x}Mg_xO_2$ films and powders. *J. Appl. Phys.* **2001**, *89*, 8022–8025. [CrossRef]
82. Tripathi, T.S.; Niemelä, J.-P.; Karppinen, M. Atomic layer deposition of transparent semiconducting oxide $CuCrO_2$ thin films. *J. Mater. Chem. C* **2015**, *3*, 8364–8371. [CrossRef]
83. Chikoidze, E.; Boshta, M.; Gomaa, M.; Tchelidze, T.; Daraselia, D.; Japaridze, D.; Shengelaya, A.; Dumont, Y.; Neumann-Spallart, M. Control of p-type conduction in Mg doped monophase $CuCrO_2$ thin layers. *J. Phys. D Appl. Phys.* **2016**, *49*, 205107. [CrossRef]
84. Rastogi, A.C.; Lim, S.H.; Desu, S.B. Structure and optoelectronic properties of spray deposited Mg doped *p*-$CuCrO_2$ semiconductor oxide thin films. *J. Appl. Phys.* **2008**, *104*, 023712. [CrossRef]
85. Lim, S.H.; Desu, S.; Rastogi, A.C. Chemical spray pyrolysis deposition and characterization of P-type $CuCr_{1-x}Mg_xO_2$ transparent oxide semiconductor thin films. *J. Phys. Chem. Solids* **2008**, *69*, 2047–2056. [CrossRef]
86. Le Trong, H.; Bui, T.M.A.; Presmanes, L.; Barnabé, A.; Pasquet, I.; Bonningue, C.; Tailhades, P. Preparation of iron cobaltite thin films by RF magnetron sputtering. *Thin Solid Films* **2015**, *589*, 292–297. [CrossRef]
87. Lalanne, M.; Barnabé, A.; Mathieu, F.; Tailhades, P. Synthesis and Thermostructural Studies of a $CuFe_{1-x}Cr_xO_2$ Delafossite Solid Solution with $0 \leq x \leq 1$. *Inorg. Chem.* **2009**, *48*, 6065–6071. [CrossRef] [PubMed]
88. Chiu, T.W.; Tsai, S.W.; Wang, Y.P.; Hsu, K.H. Preparation of *p*-type conductive transparent $CuCrO_2$:Mg thin films by chemical solution deposition with two-step annealing. *Ceram. Int.* **2012**, *38*, S673–S676. [CrossRef]
89. Lin, C.; Wang, J. Sol–gel preparation of delafossite CuCr1-x Mgx O2 thin films by nitrate salts. *Mater. Lett.* **2016**, *165*, 111–114. [CrossRef]
90. Götzendörfer, S.; Löbmann, P. Influence of single layer thickness on the performance of undoped and Mg-doped $CuCrO_2$ thin films by sol–gel processing. *J. Sol-Gel Sci. Technol.* **2011**, *57*, 157–163. [CrossRef]
91. Scanlon, D.O.; Watson, G.W. Understanding the p-type defect chemistry of $CuCrO_2$. *J. Mater. Chem.* **2011**, *21*, 3655. [CrossRef]
92. Ingram, B.J.; Gonzá Lez, G.B.; Mason, T.O.; Shahriari, D.Y.; Barnabé, A.; Ko, D.; Poeppelmeier, K.R. Transport and Defect Mechanisms in Cuprous Delafossites. 1. Comparison of Hydrothermal and Standard Solid-State Synthesis in $CuAlO_2$. *Chem. Mater.* **2004**, *14*, 5616–5622. [CrossRef]
93. Ingram, B.J.; Bertoni, M.I.; Poeppelmeier, K.R.; Mason, T.O. Point defects and transport mechanisms in transparent conducting oxides of intermediate conductivity. *Thin Solid Films* **2005**, *486*, 86–93. [CrossRef]
94. Norton, E.; Farrell, L.; Callaghan, S.D.; McGuinness, C.; Shvets, I.V.; Fleischer, K. X ray spectroscopic studies of the electronic structure of chromium based p type transparent conducting oxides. *Phys. Rev. B* **2016**, *93*, 115302. [CrossRef]
95. Mott, N.F.; Davis, E.A. *Electronic Processes in Non-Crystalline Materials*; Oxford University Press: Oxford, UK, 1979.
96. Jonker, G.H. The application of combined conductivity and Seebeck effet plots for the analysis of semiconductor properties. *Philips Res. Rep.* **1968**, *23*, 131–138.

97. Tauc, J. Optical properties and electronic structure of amorphous Ge and Si. *Mater. Res. Bull.* **1968**, *3*, 37–46. [CrossRef]
98. Ebraheem, S.; El-Saied, A. Band Gap Determination from Diffuse Reflectance Measurements of Irradiated Lead Borate Glass System Doped with TiO_2 by Using Diffuse Reflectance Technique. *Mater. Sci. Appl.* **2013**, *4*, 324–329.
99. Kaya, I.C.; Sevindik, M.A.; Akyıldız, H. Characteristics of Fe- and Mg-doped $CuCrO_2$ nanocrystals prepared by hydrothermal synthesis. *J. Mater. Sci. Mater. Electron.* **2016**, *27*, 2404–2411. [CrossRef]
100. Mott, N.F. *Conduction in Non-Crystalline Materials*; Oxford University Press: Oxford, UK, 1987.
101. Chaikin, P.M.; Beni, G. Thermopower in the correlated hopping regime. *Phys. Rev. B* **1976**, *13*, 647–651. [CrossRef]
102. Heikes, R.R.; Ure, R.W. *Thermoelectricity: Science and Engineering*; Interscience Publishers: Olney, UK, 1961.
103. Scanlon, D.O.; Godinho, K.G.; Morgan, B.J.; Watson, G.W. Understanding conductivity anomalies in Cu-I-based delafossite transparent conducting oxides: Theoretical insights. *J. Chem. Phys.* **2010**, *132*, 24707. [CrossRef] [PubMed]

© 2017 by the authors. Licensee MDPI, Basel, Switzerland. This article is an open access article distributed under the terms and conditions of the Creative Commons Attribution (CC BY) license (http://creativecommons.org/licenses/by/4.0/).